Research Square

Preprints are preliminary reports that have not undergone peer review.
They should not be considered conclusive, used to inform clinical practice,
or referenced by the media as validated information.

Electronic Bands and Altermagnetic State Modulation in a Se-Rich In_2Se_4/Cr_2SeO Heterostructure

Dan Berco

dan.berco@wsu.edu

Washington State University https://orcid.org/0000-0003-2902-1422

Research Article

Keywords: Altermagnetism, Cr_2SeO, In_2Se_4, Spin-polarized electronic band structure, Density functional theory, Orbital hybridization

Posted Date: November 9th, 2026

DOI: https://doi.org/10.21203/rs.3.rs-11640927/v1

License: This work is licensed under a Creative Commons Attribution 4.0 International License.
Read Full License

Additional Declarations: The authors declare no competing interests.

Electronic Bands and Altermagnetic State Modulation in a Se-Rich In_2Se_4/Cr_2SeO Heterostructure

Authors

Dan Berco[1,*]

Affiliations

[1] School of Electrical Engineering & Computer Science, Washington State University, 355 NE Spokane St, Pullman, WA, 99163, USA

Correspondence to:

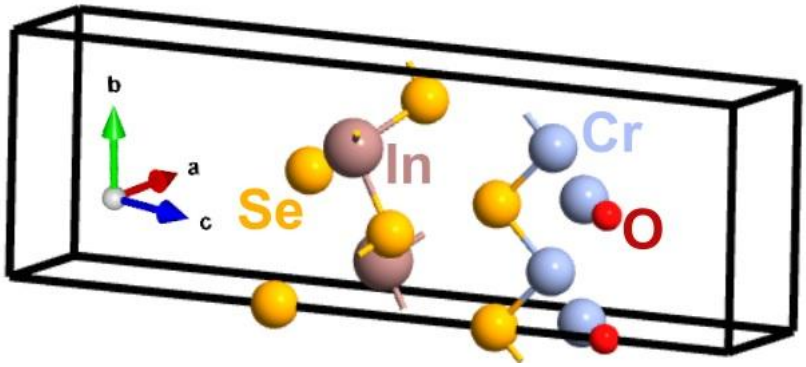
* D.B, danny.barkan@gmail.com

Abstract

Two-dimensional van der Waals (vdW) heterostructures provide a versatile platform for engineering electronic properties through interfacial charge redistribution and orbital hybridization. In this work, a Se-rich-designated In_2Se_4/Cr_2SeO vdW heterostructure is proposed and investigated using density functional theory. The In_2Se_4 layer serves as an electronically active interface in which the enhanced selenium sublattice provides Se-*p* states capable of interacting with the Cr-3*d*-derived states of an altermagnetic Cr_2SeO. A 1×1×1 In_2Se_4 monolayer and a strained (tensile in x and compressive in y) 1×2×1 Cr_2SeO cell were used to construct a supercell. The structural stability of the heterostructure is first evaluated through relaxation. The electronic properties are then characterized using spin-resolved band structures, projected density of states, orbital-resolved electronic states, and spatial charge density. The calculations reveal that interlayer coupling substantially modifies the electronic states near the Fermi level while retaining the characteristic spin-dependent structure of the Cr_2SeO layer. Overall, the heterostructure exhibits momentum-dependent semi-metallic/semiconducting behavior with strongly spin-selective local gaps. Se displacement in the In_2Se_4 monolayer acts as a symmetry and electrostatic control parameter that modifies the spin channels differently at different k-points. The resulting

momentum-selective modification of Cr-derived states demonstrates the potential of Se-rich chalcogenide interfaces for tailoring the electronic structure of two-dimensional altermagnets. These findings suggest this heterostructure as a promising platform for investigating interfacial spin-dependent phenomena, provide insight into low-dimensional magnetic materials, and provide a theoretical foundation for nanoscale spintronic applications.

Keywords: Altermagnetism, Cr_2SeO, In_2Se_4, Spin-polarized electronic band structure, Density functional theory, Orbital hybridization.



Graphical TOC. Density functional theory analysis reveals that a Se-rich In_2Se_4 interface substantially modifies the spin-dependent electronic structure of altermagnetic Cr_2SeO through interfacial charge redistribution and Se-*p*/Cr-*d* hybridization. The predicted momentum-selective modulation suggests In_2Se_4/Cr_2SeO as a promising platform for engineering electronic properties in two-dimensional magnetic heterostructures.

INTRODUCTION

Altermagnetism has recently emerged as a distinct magnetic phase that combines properties of both ferromagnets and antiferromagnets. Like conventional antiferromagnets, altermagnets feature a fully compensated magnetic order with zero net macroscopic magnetization. However, unlike conventional ferromagnets, altermagnets can exhibit substantial spin polarization without a macroscopic net magnetization, while their spin degeneracy is lifted by the system's crystal and magnetic symmetries.[1-3] The strong dependence of altermagnetic electronic states on crystal symmetry, strain, and interfacial interactions makes two-dimensional altermagnets particularly attractive for Altermagnetic Tunnel Junctions & Memory,[4, 5] Spin Field-Effect Transistors,[6, 7] Spin-Transfer Torque & Logic Devices,[8, 9] and even Device-dedicated Robotic Vision.[10-14] Among recently proposed two-dimensional altermagnets, Janus Cr_2SeO is especially promising because it combines altermagnetism, ferroic properties, and strain-dependent electronic behavior. First-principles calculations have predicted substantial spin splitting of approximately 0.38 eV at the X and Y high-symmetry points, together with ferroelectricity, piezo-valley effects, and tunable magnetic properties under strain.[15] These characteristics suggest that modifying the Cr_2SeO chemical and electrostatic environment could provide an effective route for controlling its momentum-dependent spin-polarized electronic states.

Van der Waals (vdW) heterostructures provide a convenient platform for such interface engineering because atomically thin layers with distinct electronic properties can be combined without requiring conventional covalent bonding. Interfacial charge redistribution, electrostatic potential differences, and orbital hybridization can substantially alter the electronic structure of the constituent layers. Hybridization between chalcogen *p* states and transition-metal *d* states provides a direct mechanism for modifying band dispersion and spin-dependent states at the interface. Indium selenides are particularly interesting in this context. Monolayer α-In_2Se_3 has been predicted and experimentally investigated as a two-dimensional ferroelectric semiconductor with switchable out-of-plane polarization.[16, 17]

Its polarization is strongly coupled to the in-plane structural configuration, providing an additional structural degree of freedom for controlling electronic properties.[17] These characteristics have motivated extensive investigation of In_2Se_3-based vdW heterostructures and their interfacial electronic behavior.

The relationship between ferroic structural degrees of freedom and altermagnetism has recently attracted considerable attention. Gu *et al.* demonstrated theoretically that reversal of ferroelectric polarization can be coupled to reversal of altermagnetic spin-splitting, establishing the concept of ferroelectric-switchable altermagnetism.[18] More recent work has expanded this concept to other ferroic degrees of freedom, including ferroelasticity, demonstrating the broader potential of structural control of altermagnetic states.[19] These developments motivate the exploration of new chemically engineered interfaces capable of modifying the electronic structure of two-dimensional altermagnets.

This work features a density functional theory (DFT) [20, 21] study of a vdW heterostructure comprising a 1×1×1 In_2Se_4 monolayer and a 1×2×1 Cr_2SeO cell, which were used to construct a supercell to investigate the interfacial modification of the structural, electronic, and spin-dependent properties of Cr_2SeO. The two constituent layers were separated by a 3.5 Å interlayer distance, representing the vdW spacing, and 20 Å of vacuum was introduced along both the positive and negative z (c) directions to suppress interactions between periodically repeated heterostructures. The In_2Se_4 monolayer may be used to achieve in-plane lattice matching between the two components. In this manner, the Cr_2SeO 1×2×1 cell was subjected to 12% tensile strain along the x (a) direction and 3.2% compressive strain in the y (b) direction. First, the stability of the combined In_2Se_4/Cr_2SeO interface was examined following structural relaxation. The atomic positions and interlayer geometry were subsequently optimized to obtain the relaxed heterostructure configuration.

To investigate the sensitivity of the interfacial electronic structure to out-of-plane structural perturbations, spin-resolved band-structure calculations were performed for three structural displacement configurations in which the relevant Se layer was displaced along the z direction

by 0 Å, +0.5 Å (positive, marked P_+), and -0.5 Å (negative, marked P_-) relative to the initial structure (reference, marked P_0). These configurations were introduced as controlled structural perturbations to examine the resulting changes in the local electrostatic environment and interfacial orbital interactions. Comparison of the three configurations was used to evaluate displacement-dependent changes in the band dispersion, band-edge positions, spin-dependent electronic states, and local direct gap characteristics. This analysis provides insight into how out-of-plane Se-layer displacement can modulate the electronic structure of the In_2Se_4/Cr_2SeO heterostructure and the momentum-dependent spin states associated with the Cr_2SeO layer.

RESULTS AND DISCUSSION

Architectural Concept

DFT calculations in this work were performed on three different supercell structures marked P_0, P_+, and P_-. Each structure constitutes a supercell having one In_2Se_4 unit cell and two strained Cr_2SeO cells stacked in the y (b) direction. In_2Se_4 is considered here as a Se-rich interfacial structural concept motivated by the increased Se sublattice available for interfacial interaction with Cr-derived states. The present calculations examine whether such a Se-rich interface can provide a computationally viable route for modifying the electronic and spin-dependent properties of Cr_2SeO. The construction of each building block is shown in **Fig. 1**. A detailed overview of the entire structure is provided in the next section. The electronic properties were calculated for each case and compared. These structures differ by a displacement of the Se in the In_2Se_4 cell along the z (c) axis and were used to evaluate the sensitivity of the interfacial electronic structure to out-of-plane structural perturbations. For P_0, the displacement was zero, while for P_+ and P_-, the displacement was +0.5 Å and -0.5 Å, respectively.

Ball-and-stick diagrams of an orthogonal In_2Se_4 cell (using an orthorhombic transformation matrix) are shown in **Fig. 1a**, **Fig. 1b**, and **Fig. 1c**. The figures display all the equivalent atoms from different perspectives. The cell's dimensions in Å are roughly 4.16×7.20×5.86. A

ball-and-stick diagram of two stacked Orthogonal Cr_2SeO cells is shown in **Fig. 1d**, **Fig. 1e**, and **Fig. 1f**. The dimensions in Å of a single Orthogonal Cr_2SeO are 3.72×3.72×6.0. Due to lattice mismatch, a single (1×1×1) In_2Se_4 with two (1×2×1) Cr_2SeO therefore generates a 3.2% compressive strain (7.20/7.44) in the b-direction, and a ~12% (4.16/3.72) tensile strain in the a-direction.

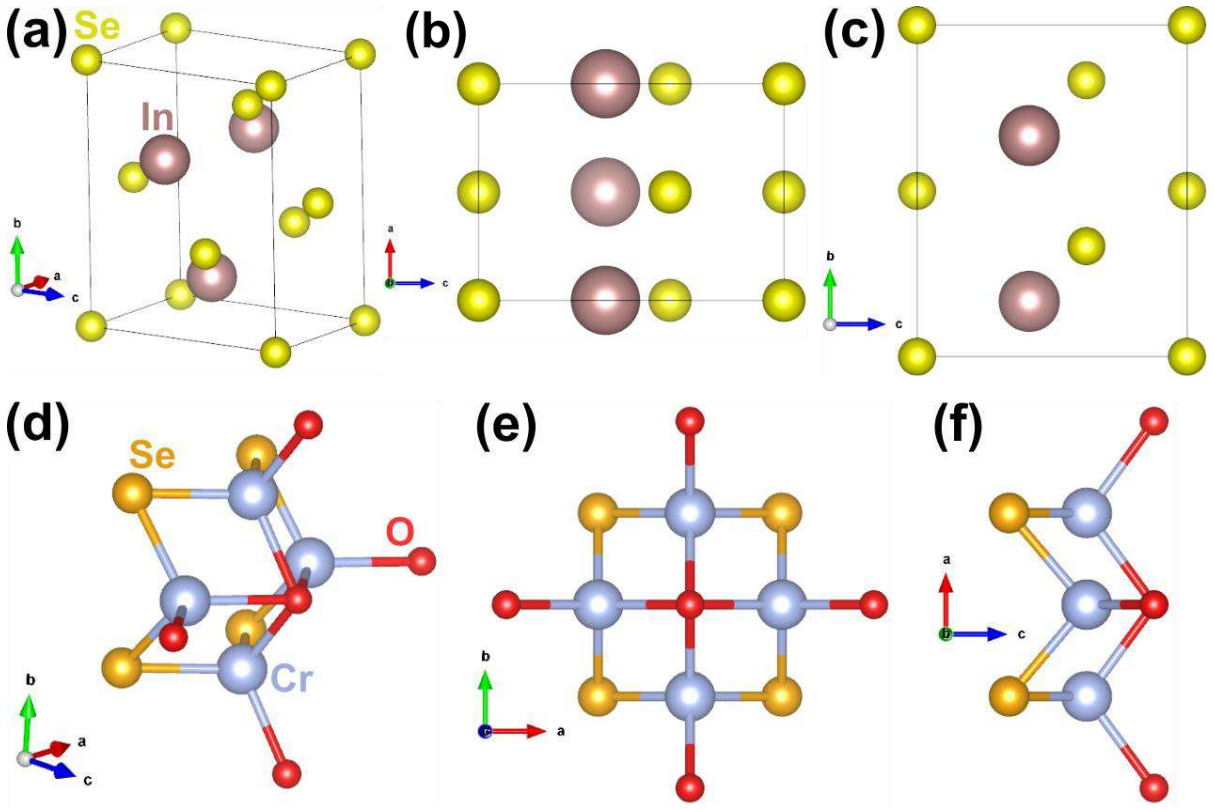


Fig. 1. Ball-and-stick diagram of the building blocks used in the simulated structures, with all equivalent atoms displayed. **(a)** A 3D view of a single Orthogonal In_2Se_4. **(b)** In_2Se_4 from the a-c plane perspective. **(c)** In_2Se_4 from the b-c plane perspective. **(d)** A 3D view of two stacked Orthogonal Cr_2SeO cells. **(e)** Cr_2SeO from the a-b plane perspective. **(f)** Cr_2SeO from the a-c plane perspective.

Since the two constituent monolayers possess different equilibrium lattice dimensions, direct construction of a low-periodicity heterostructure without lattice adjustment would result in significant structural mismatch. The selected strain therefore represents a deliberate interface-engineering condition rather than an arbitrary perturbation, enabling a periodic In_2Se_4/Cr_2SeO interface to be modeled within a computationally tractable supercell. More importantly, the applied tensile strain is also physically relevant because strain can substantially modify the orbital hybridization, band dispersion, and momentum-dependent

spin splitting of Cr_2SeO. The corresponding 3.2% compressive strain along the y direction and 12% tensile along the x direction provide the complementary lattice adjustment required by the heterostructure geometry. The resulting anisotropic strain state therefore allows the effects of interfacial lattice matching and strain-induced electronic modulation to be examined.

Structural Relaxation

DFT tools are used to gain a deeper understanding of atomic-level electronic properties such as band structure and quantum transport. The physical timescale of DFT is computationally limited to electronic relaxations on the femtosecond scale. The following literature offers detailed investigations into extended temporal scales.[22, 23] The current work aims to provide further insight into atomic-level electronic properties analysis. This section covers structural relaxation of the supercell model. In this study, a vdW heterostructure comprising a 1×1×1 In_2Se_4 monolayer and a 1×2×1 Cr_2SeO cell was used to construct a supercell to investigate the electronic properties. The two constituent layers were separated by a 3.5 Å interlayer distance, representing the vdW spacing, and 20 Å of vacuum was introduced along both the positive and negative c-directions. The total length of the supercell was thus ~52 Å.

Once an initial placement was made, the whole cell underwent a structural relaxation. The relaxation process is based on a time-domain simulation that executes molecular dynamics algorithms. The process is completed at an equilibrium point of the microcanonical ensemble once the calculated energy drops below a predetermined value. The classical equation of motion for a system with *N* particles is (indexed as *i=1, 2..N*):

$$m_i \frac{d^2\vec{r}_i}{dt^2} = \vec{f}_i \quad (1)$$

With *m* the mass, *f* the force, and *r* the location vector. If the particles are interacting through a potential *v*, the Hamiltonian can be written with the momentum *p* as:

$$\dot{\vec{p}}_i = -\nabla_{\vec{r}_i} v = \vec{f}_i \quad (2)$$

The time evolution of this system is governed by fundamental conservation laws. With the Hamiltonian *H,* we can write:

$$\frac{dH}{dt} = \frac{\partial H}{\partial t} + \frac{\partial H}{\partial \vec{p}}\frac{\partial \vec{p}}{\partial t} + \frac{\partial H}{\partial \vec{q}}\frac{\partial \vec{q}}{\partial t} = 0 \quad (3)$$

Calculating the time-dependent trajectories involves either solving a set of *3N* second-order differential equations or a set of *6N* first-order equations. The system may be considered relaxed once the total energy is minimized. The heterostructure was fully relaxed until the maximum residual force was below 0.01 eV $Å^{-1}$, using a maximum ionic displacement of 0.1 Å per optimization step.

The 12% tensile strain was selected to achieve commensurability between the In_2Se_4 and Cr_2SeO lattices within the chosen low-periodicity supercell. To assess whether this strain remains physically meaningful, the strained supercell was evaluated through full structural relaxation. The In_2Se_4/Cr_2SeO interface remained structurally intact without spontaneous separation or major reconstruction. This absence of significant structural instability under the applied strain supports its use as an interface-engineering configuration. The complete structure is shown in **Fig. 2**. The figure shows atomic positions in the cell in the pre (**Fig. 2a**) and post (**Fig. 2b**) relaxation configurations. The system reached the predetermined steady state after about 25 steps. **Fig. 2c** shows the energy, and **Fig. 2d** shows the total forces.

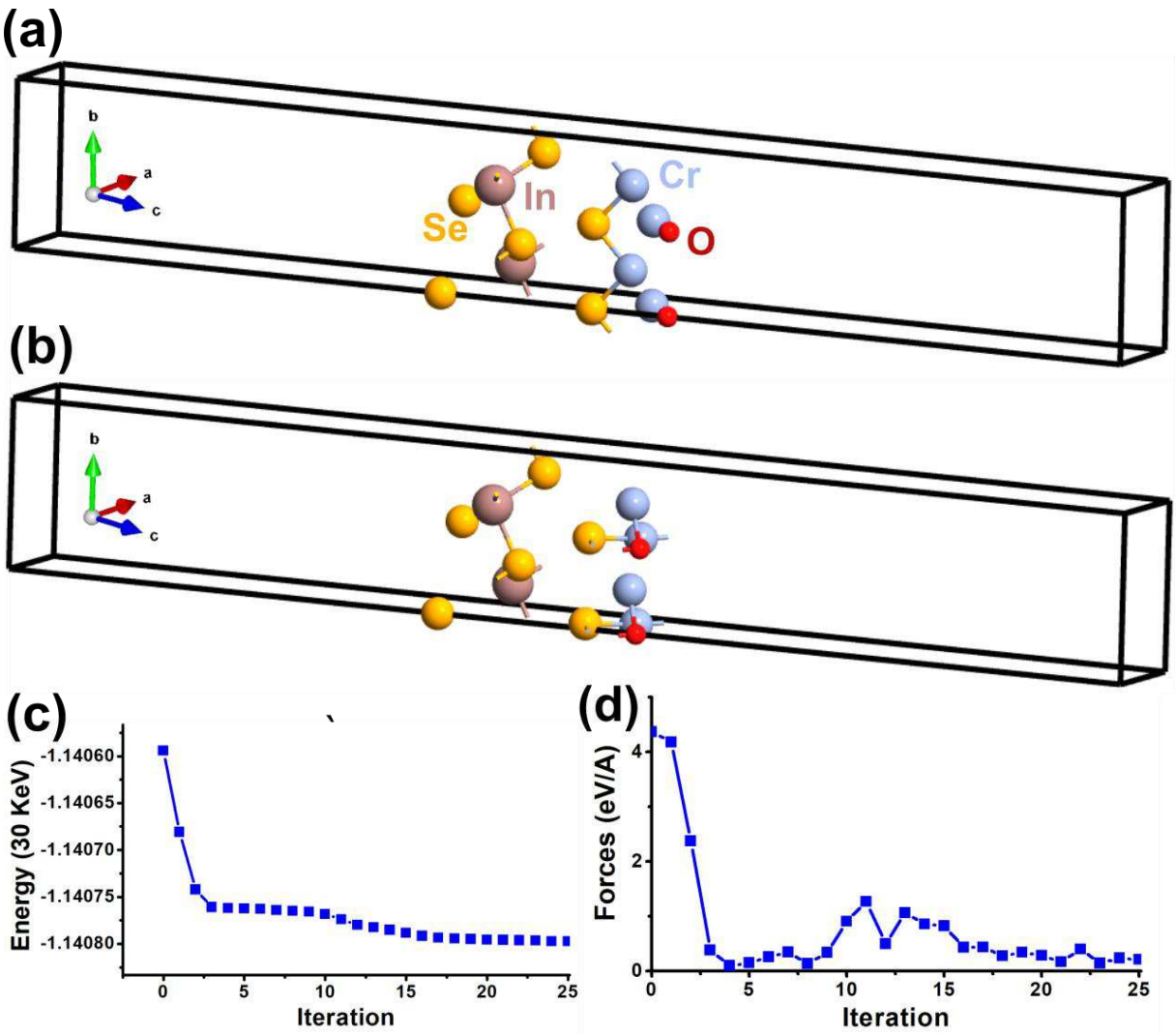


Fig. 2. Structural relaxation: A 1×1×1 In_2Se_4 combined with strained 1×2×1 Cr_2SeO (equivalent atoms hidden) to a supercell with 20 Å of vacuum along the c direction on either end. **(a)** Pre-relaxation supercell. **(b)** Post-relaxation supercell. **(c)** Overall energy vs. iteration number. **(d)** Total forces vs. iteration number.

Strained Cr_2SeO Band Structure

All calculations were based on the software's built-in linear combination of atomic orbitals (LCAO) calculator.[24, 25] In molecular orbital theory, this concept describes the way atomic orbitals combine to form molecular orbitals. These orbitals are described by a basis set that is an integral part of the DFT software.[26] Molecular orbitals are formed by taking linear combinations as weighted sums of these atomic orbitals to form the overall function Ψ according to:

$$\Psi_{MO} = \sum_{i=1}^{N} c_i \varphi_i \qquad (4)$$

With $i=1..N$ elements, c_i the corresponding weight, and φ_i the individual orbital. In this work, calculations were based on combining the Spin-polarized Generalized Gradient Approximation (SGGA),[27] the Perdew-Burke-Ernzerhof (PBE) exchange-correlation functional,[28] and an added Hubbard U correction term [29] to fix electron over-delocalization in localized *d* or *f* orbitals. The total exchange-correlation energy in SGGA accounts for both the local spin densities and their spatial variations and is given by:

$$E_{xc}^{SGGA} = \int \rho \cdot \varepsilon_{xc(\rho\uparrow,\rho\downarrow,\nabla\rho\uparrow,\nabla\rho\downarrow)} F_{xc} d^3r \quad (5)$$

Where ε_{xc} represents the exchange-correlation energy per electron for a uniform electron gas, F_{xc} is an enhancement factor, and $\rho_{(r)} = \rho_{\uparrow} + \rho_{\downarrow}$ is the total density of spin-up and spin-down components. The PBE functional splits the energy into individual exchange and correlation components:

$$E_{xc}^{PBE} = E_x^{PBE} + E_c^{PBE} \quad (6)$$

With *Ex* being the exchange term and *Ec* the correlation term. The PBE exchange energy:

$$E_x^{PBE} = \sum_{\sigma=\uparrow,\downarrow} [\int \varepsilon_{xc} \rho_\sigma p_x d^3r] \quad (7)$$

With the enhancement factor p_x . The PBE correlation energy is evaluated as:

$$E_c^{PBE} = \int \rho [\varepsilon_{xc} + H] d^3r \quad (8)$$

where *H* is the non-local correlation gradient correction term.

Fig. 3 illustrates the calculated band structure of a standalone, pristine, 1×2×1 Cr_2SeO structure, as well as for a strained (3.2% compressive strain along the b-direction, and a 12% tensile strain in the a-direction) 1×2×1 structure. Both images are centered around the Fermi level (marked as ε_f) with a ±2 eV spread. The band structure in **Fig. 3a** is similar to the one reported by Li *et al*.[5] where a separation of spin-state energy bands is observed around the Fermi level. In this work, band no. 25, representing the conduction band, shows two distinct minima for up and down spin states at reciprocal lattice points Y and X, respectively. On the other hand, band no. 24, representing the valence band, shows two distinct maxima for up and

down spin states at reciprocal lattice points X and Y.

The band structure in **Fig. 3b** was calculated for the strained structure. It has several distinct differences from the pristine case. First, the symmetry between X and Y was broken due to the applied strain. In this case, the local gap at X was about 0.3 eV, while the local gap at Y grew to over 1.1 eV. Second, the band structure at X and S was made of spin-up levels and not opposite spin polarities as in **Fig. 3a**. Third, ε_f was shifted much closer to the valence band at X and to the conduction band at S. These effects suggest potential relevance for spintronic applications.

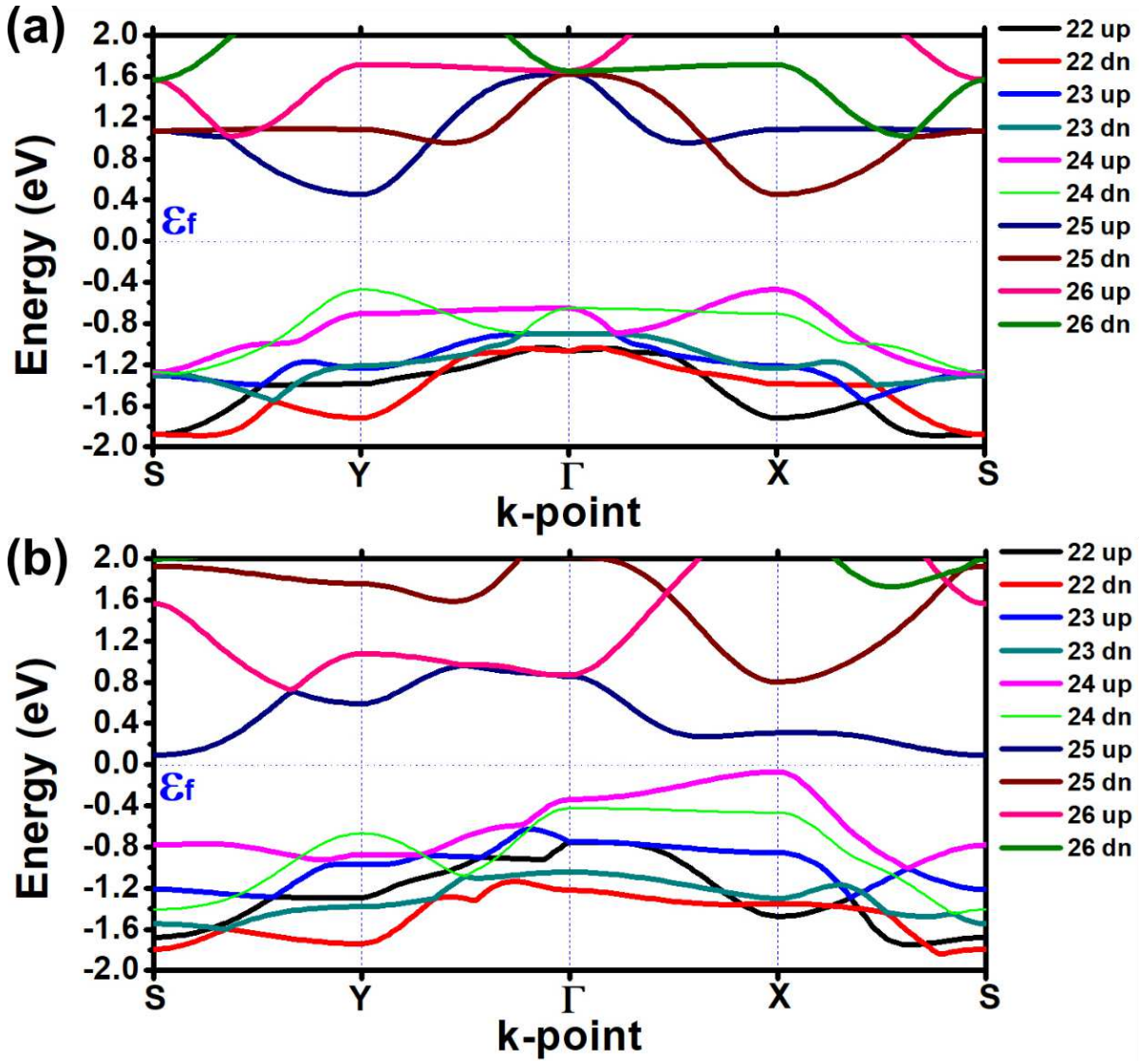


Fig. 3. Band structure of a standalone 1×2×1 Cr_2SeO structure. **(a)** Unstrained 3.72×7.44×6.0 ($Å^3$). **(b)** Strained 4.16×7.20×6.0 ($Å^3$).

In_2Se_4/Cr_2SeO Supercell Spin Distribution

Understanding the spatial spin distribution in the supercell would be a useful foundation in this work. **Fig. 4** illustrates the total spin within the supercell projected onto the y-z (b-c) plane. The black dots represent atomic placements, with annotations indicating atomic types. The dashed green line shows the initial z-coordinate of Se in the In_2Se_4 monolayer (P_0 in **Fig. 4a**). In the following sections, the effects of positive (P_+ in **Fig. 4b**) and negative (P_- in **Fig. 4c**) is presented. The green arrows indicate the directions of those shifts. A maximal displacement of 0.5 Å was used in this work. The ±0.5 Å range was selected as a controlled structural perturbation to probe the sensitivity of the interfacial bands. The figure shows how the spatial spin varies between values of ±5, corresponding to the Cr-3*d*-derived states of an altermagnetic Cr_2SeO. In other regions of the supercell, the average spin is virtually zero, indicating that mainly the Cr_2SeO layer could be utilized in spin transport since the magnetic degrees of freedom remain spatially localized in Cr_2SeO while the nonmagnetic In_2Se_4 layer acts primarily as an electrostatic interface modifier.

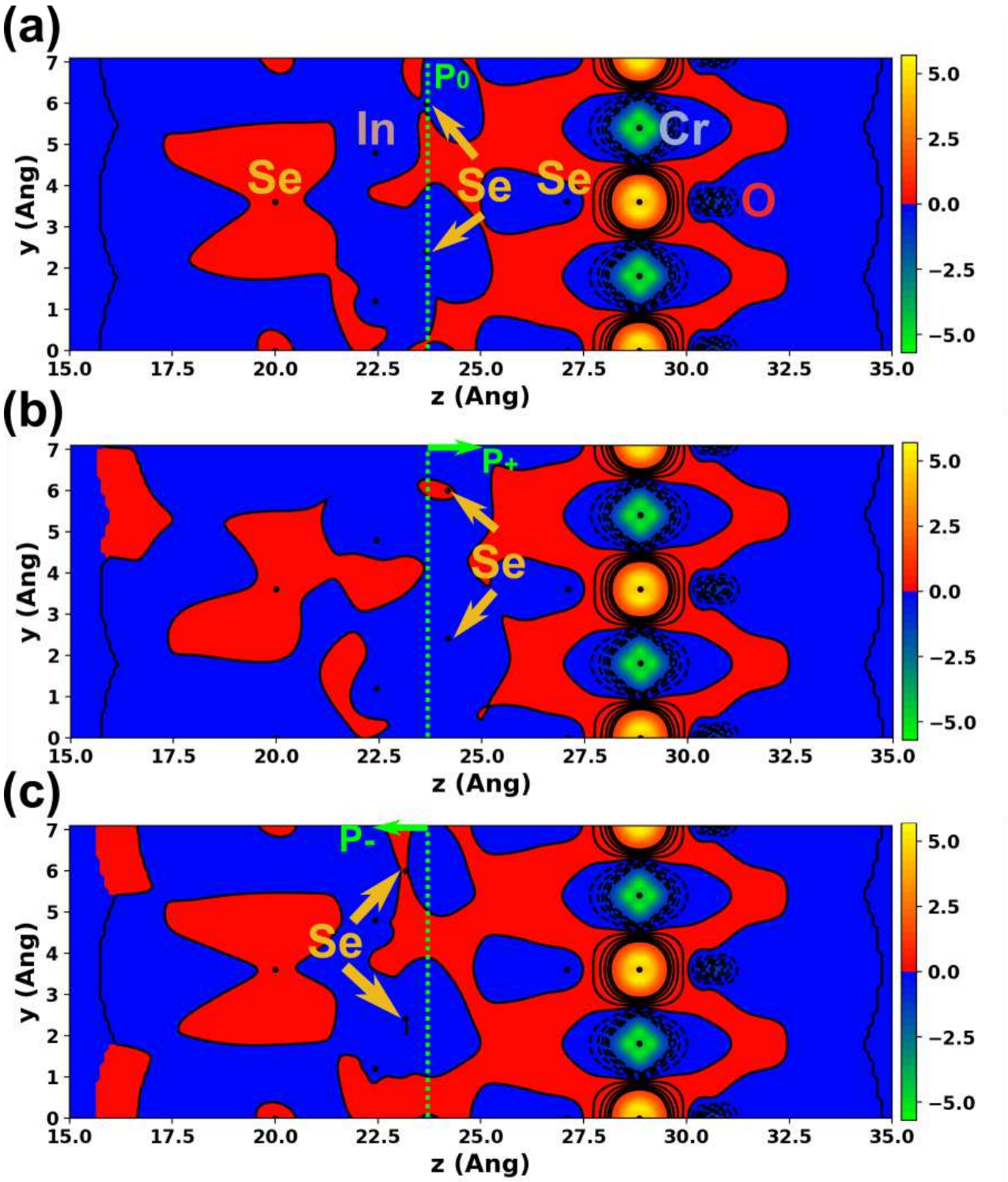


Fig. 4. Total spin projected along the y-z (b-c) plane; The dashed green line indicates the initial c-coordinate of Se in the In_2Se_4 monolayer. **(a)** P_0. **(b)** P_+. **(c)** P_-.

Unrelaxed Supercell Band Structure

The ball-and-stick models in **Fig. 5a** and **Fig. 5b** depict the atomic composition of the unrelaxed In_2Se_4/Cr_2SeO supercell. The figures include equivalent atoms, so they appear slightly different from the image in **Fig. 2a**. **Fig. 5a** shows the supercell from the b-c plane

perspective. The green arrows indicate the Se displacement directions for P_+ and P_-. **Fig. 5b** shows the supercell from the a-b plane perspective. The band structures in **Fig. 5c**, **Fig. 5d**, and **Fig. 5e** correspond to P_+, P_0, and P_-, respectively. All diagrams show semi-metallic-like band structures, with ε_f crossing valence bands 94 and 95 at Γ and Y for spin down. However, in **Fig. 5c**, at the reciprocal lattice points X and S, there is a local direct gap between 95 and 96 of about 0.4 eV for spin up and about 0.8 eV for spin down at S. This spin-up gap narrows to about 0.25 eV in **Fig. 5d**. At the same time, ε_f moves toward the mid-gap and drops to zero in **Fig. 5e** as ε_f intersects with band 96 at X. At k-point S, ε_f does not reach band 96, but the gap drops to ~0.1 eV. For spin-down, the gap remains significantly larger in all three pictures.

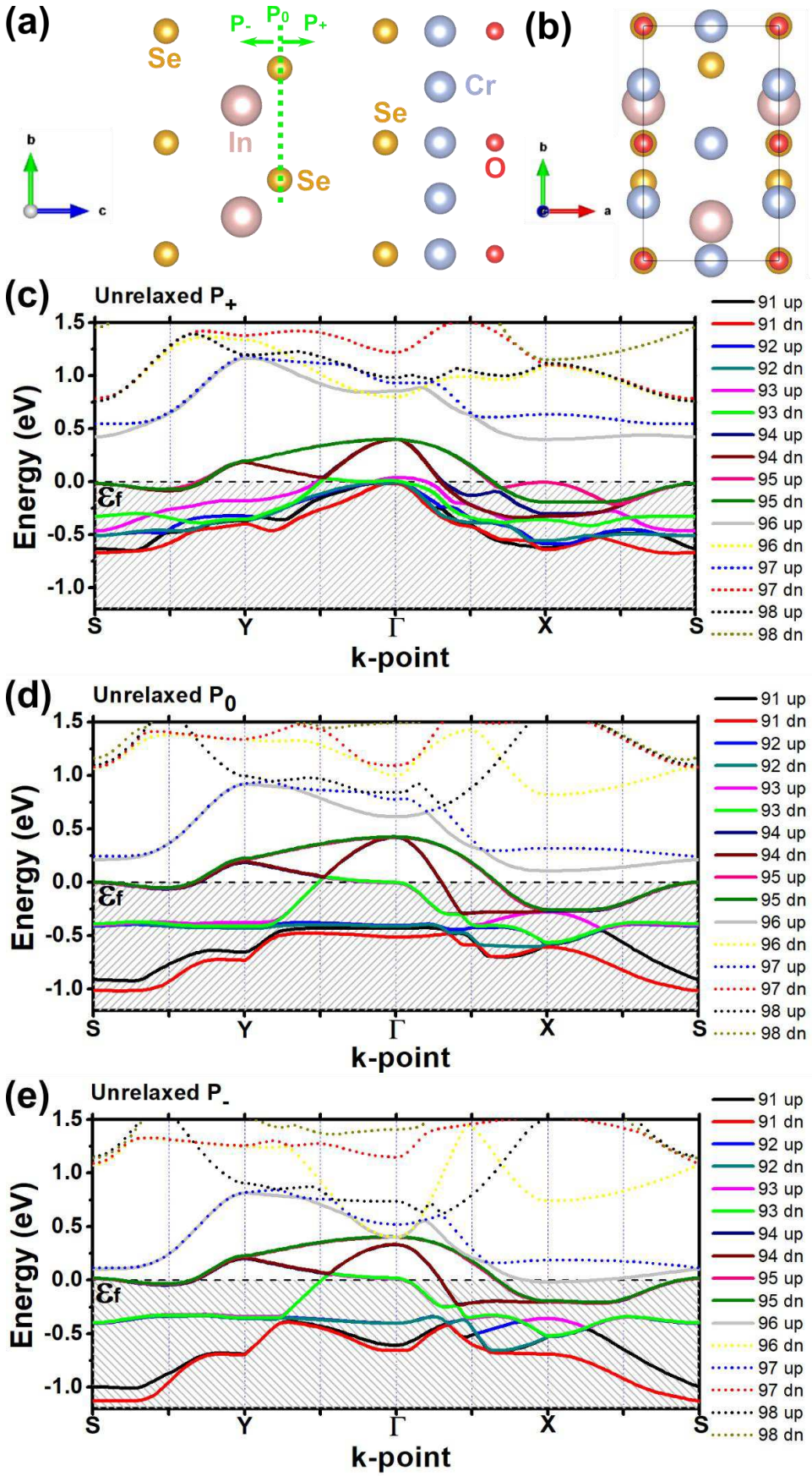


Fig. 5. Spin-dependent band diagram of the **unrelaxed** In_2Se_4/Cr_2SeO supercell with three Se placements (P_0, P_+, P_-). **(a)** Ball-and-stick diagram from the b-c plane perspective with displacement indicators as green arrows. **(b)** Ball-and-stick diagram from the a-b plane perspective. **(c)** P_+ bands. **(d)** P_0 bands. **(e)** P_- bands.

Relaxed Supercell Band Structure

The pristine and strained Cr_2SeO calculations provide a reference against which the subsequent In_2Se_4/Cr_2SeO results are compared. Changes that remain after this strain-induced baseline is established are attributed to interfacial electrostatic interactions and orbital hybridization rather than to strain alone. The ball-and-stick models of **Fig. 6a** and **Fig. 6b** depict the atomic composition of the relaxed In_2Se_4/Cr_2SeO supercell. The figures include equivalent atoms, so they appear slightly different from the image in **Fig. 2b**. **Fig. 6a** depicts the supercell from the b-c plane perspective. The green arrows indicate the Se displacement direction for P_+ and P_-. **Fig. 6b** depicts the supercell from the a-b plane perspective. The band structures of **Fig. 6c**, **Fig. 6d**, and **Fig. 6e** correspond to P_+, P_0, and P_-, respectively.

The band picture in this case differs from the one illustrated in **Fig. 5**. For **Fig. 6c** ε_f crosses spin-up band 95, therefore exhibiting semi-metallic-like properties with zero-gap states at X. On the other hand, for spin-up at X in **Fig. 6d** and **Fig. 6e**, a gap of ~0.5-1.0 eV is apparent, with ε_f placed within it. For spin-down at X, the energy gap remains consistently large in all cases. For S, ε_f intersects band 95 tangentially for both spin-up and spin-down. Both spin polarities have a relatively large gap at this point (compared to X) in all three configurations. The gap is ~0.5 eV in **Fig. 6c**, ~0.8 eV in **Fig. 6d**, and ~0.3 eV in **Fig. 6e** for both spin-up and spin-down.

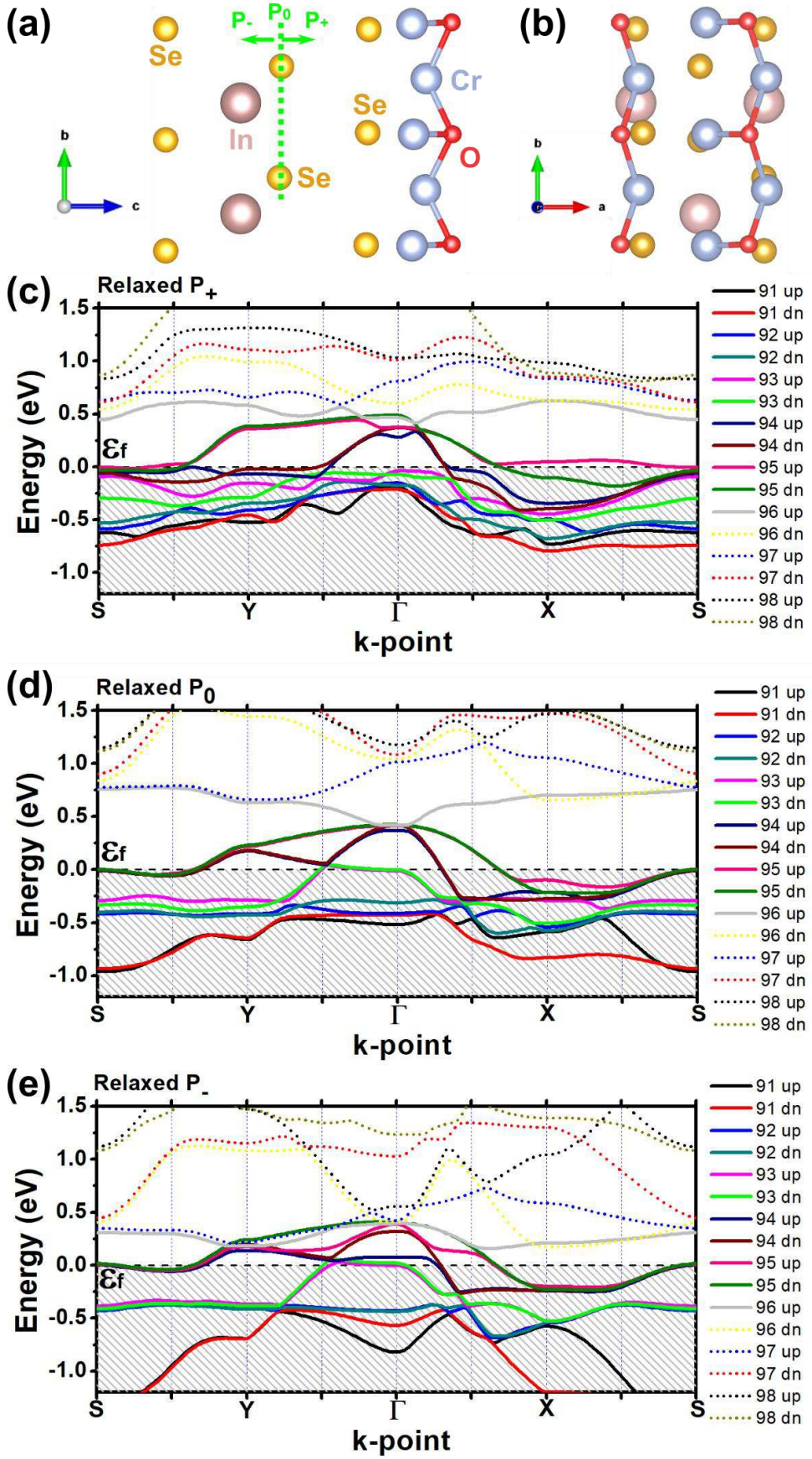


Fig. 6. Spin-dependent band diagram of the **relaxed** In_2Se_4/Cr_2SeO supercell with three Se placements (P_0, P_+, P_-). **(a)** Ball-and-stick diagram from the b-c plane perspective with displacement indicators as green arrows. **(b)** Ball-and-stick diagram from the a-b plane perspective. **(c)** P_+ bands. **(d)** P_0 bands. **(e)** P_- bands.

Momentum-Selective Spin-Dependent Band Modulation

The central electronic response of the heterostructure is the strongly asymmetric evolution of the spin-resolved states with Se-layer displacement. Rather than producing a rigid shift of the entire electronic spectrum, the displacement modifies selected Cr-derived bands differently at different points of the Brillouin zone. The results indicate that the most pronounced response occurs near X, where the spin-up band edges exhibit substantially larger energy shifts than their spin-down counterparts. In contrast, the S-point states display a qualitatively different and weaker response. This momentum-selective behavior indicates that the interfacial structural degree of freedom couples selectively to the spin-dependent electronic states of Cr_2SeO.

Spatial displacement of the Se layer produced differences in both the local energy gap and ε_f location. **Fig. 7** depicts the energetic environment of different bands, centered around ε_f, and different spin polarities, with different Se displacements at k-point X. The figure specifically shows the energy values of bands 94-97, for spin up and spin down, at point X. In a sense, this can be considered a top-of-valence and a bottom-of-conduction band diagram. The Se layer is shifted from -0.5 to 0.5 Å in steps of 0.1 Å, corresponding to induced positive and negative electric polarizations. **Fig. 7a** shows the band energies around ε_f for a positive displacement (P_+) from 0 to 0.5 Å and spin up. **Fig. 7b** shows the band energies for P_+ and spin down. **Fig. 7c** shows the band energies around ε_f for a negative displacement (P_-) from 0 to -0.5 Å and spin up. **Fig. 7d** shows the band energies for P_- and spin down.

Considering **Fig. 7a**, for spin up, ε_f approaches band 95 as the shift increases. The overall gap between bands 95 and 96 remains relatively constant. At 0 Å, ε_f lies in the gap between 95 and 96, closer to 96. At 0.5 Å, ε_f reaches the edge of band 95. The image resembles the band inversion observed in traditional metal-oxide-semiconductor devices. Considering **Fig. 7b**, for spin down, ε_f remains at roughly the same position relative to the valence and conduction bands throughout the entire range, with the local gap increased. However, the change relative to ε_f is less drastic than in **Fig. 7a**. In **Fig. 7c**, for spin up, ε_f approaches band

96 as the negative shift increases. The overall gap between bands 95 and 96 is slightly reduced. At 0.5 Å, ε_f already surpasses 96, resembling a heavily doped, metallic-like semiconductor. The energetic picture in **Fig. 7d** for spin-down is even more stable. Both the energy difference and the relative ε_f placement are constant. This overall behavior implies a selective energetic preference for spin-up electrons over spin-down ones, and a promising potential for spintronic device implementation.

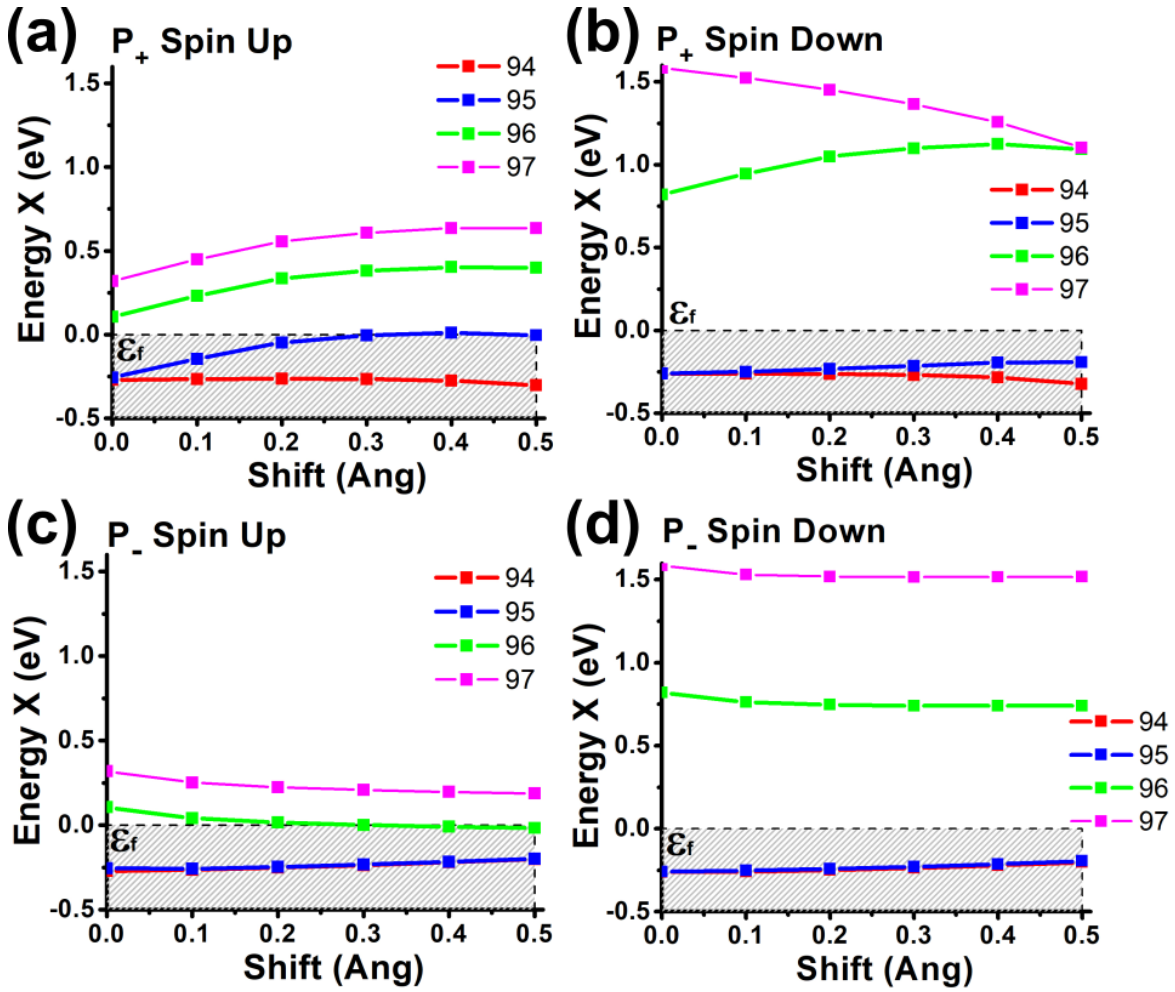


Fig. 7. X-point conduction band minima and valence band maxima dependence on Se displacement and spin polarity. **(a)** Positive displacement (P_+) with spin up. **(b)** Positive displacement (P_+) with spin down. **(c)** Negative displacement (P_-) with spin up. **(d)** Negative displacement (P_-) with spin down.

Fig. 8 depicts the energetic environment around ε_f (bands 94-97) at k-point S. **Fig. 8a** shows the energetic picture of P_+ for spin up. **Fig. 8b** shows the energetic picture of P_+ for spin down. **Fig. 8c** shows the energetic picture of P_- for spin up, and **Fig. 8d** shows the energetic picture of P_- for spin down. In all cases, ε_f overlaps the edges of bands 94 and 95.

However, the band difference increases with displacement toward the positive z-direction in both **Fig. 8a** and **Fig. 8c**. For spin-down, the gap is reduced with a positive shift (**Fig. 8b**) but remains relatively constant with a negative shift (**Fig. 8d**).

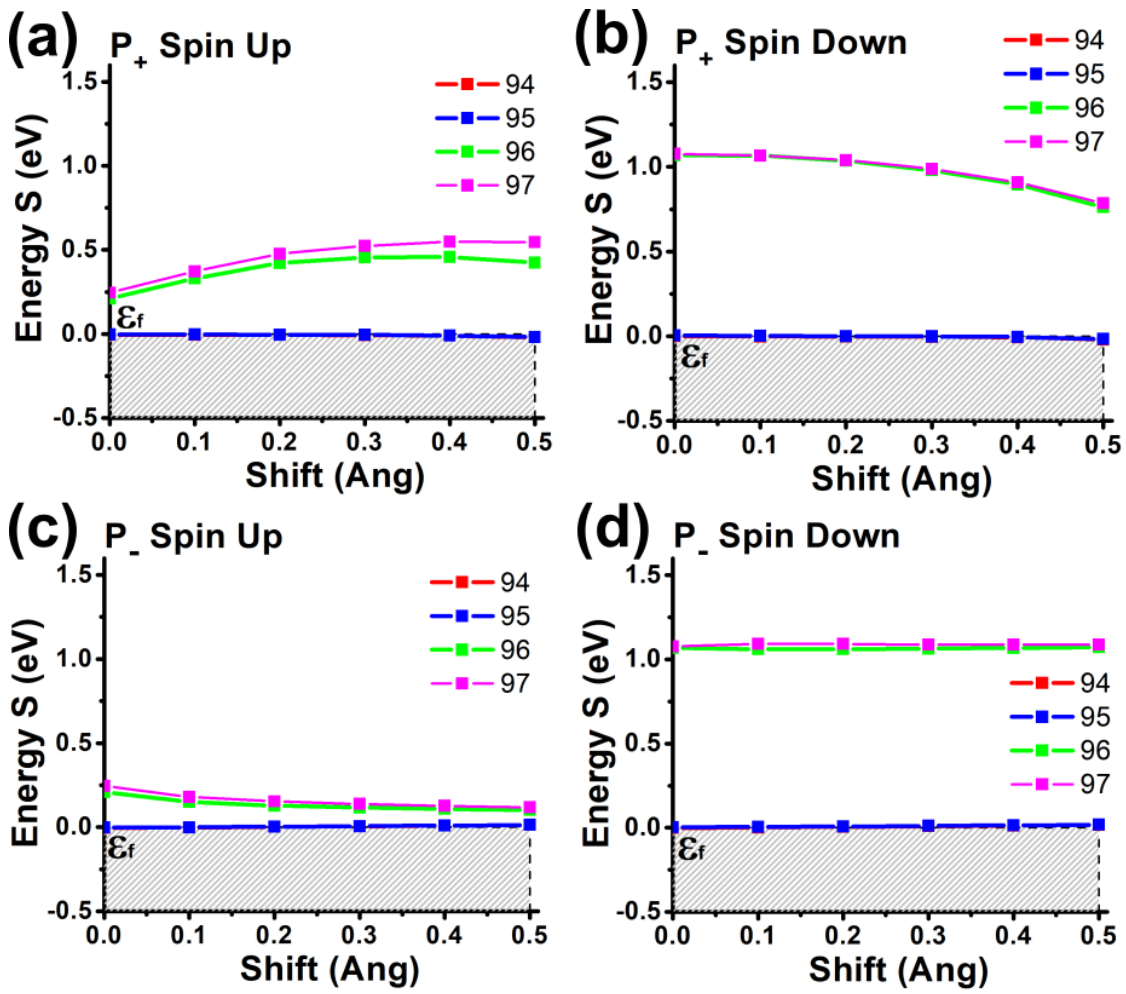


Fig. 8. S-point conduction band minima and valence band maxima dependence on Se displacement and spin polarity. **(a)** Positive displacement (P_+) with spin up. **(b)** Positive displacement (P_+) with spin down. **(c)** Negative displacement (P_-) with spin up. **(d)** Negative displacement (P_-) with spin down.

Fig. 9 summarizes the overall calculated local gap for both spin polarities, at specific points of interest in momentum space. **Fig. 9a** shows the calculated local gap at X, and **Fig. 9b** shows the gap at S. In **Fig. 9a**, the gap grows at X as the Se is displaced along the positive z (c) direction. In addition, the gap for down spin is significantly larger than the one for up spin. The gap at S shows a different behavior. **Fig. 9b** indicates that this gap is reduced for spin-down, as the Se is displaced along the positive z (c) direction. The overall gap associated with spin-down is also much larger compared to the gap for spin-up. These results imply that

different semiconducting-like properties may be achieved through such structural manipulations.

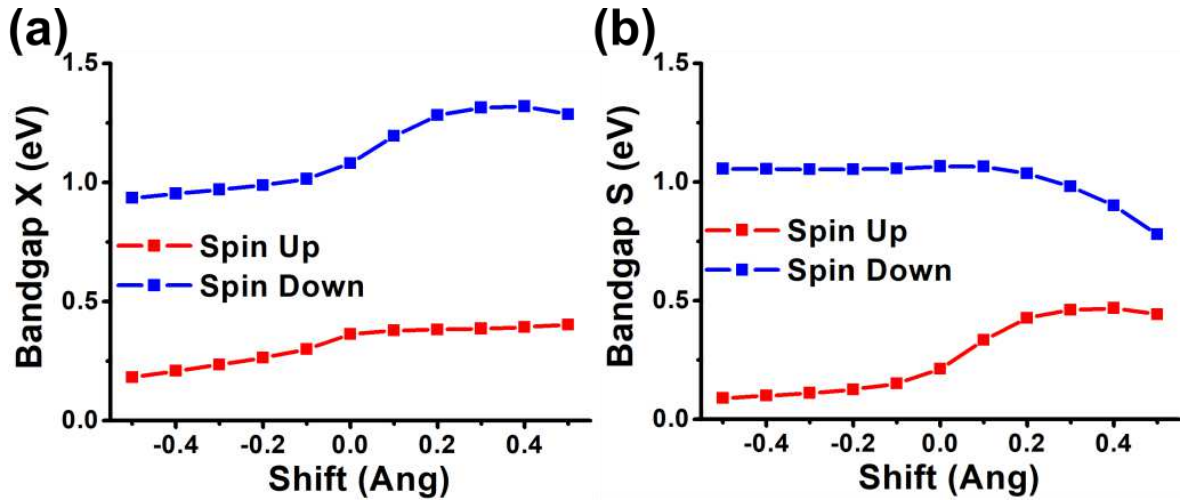


Fig. 9. Local gap vs. Se displacement for up and down spins. **(a) X-point**. **(b) S-point**.

Density of States

DFT can be used to evaluate the density of states (DOS) as the energy-resolved spectral density. It identifies which atoms and associated orbitals add conduction channels and bias-induced changes in orbital energies. Atomic and orbital resolution is used to project total DOS onto specific atoms or angular momentum channels. With i indicating specific atomic orbitals, we can write the DOS projected onto localized atomic orbitals (ϕ_i) and the n-th Kohn-Sham wave function (ψ_n):

$$DOS_{(E)} = \sum_n |\langle \phi_i | \psi_n \rangle|^2 \cdot \delta_{(E-E_n)} \qquad (9)$$

Fig. 10 depicts the combined projected DOS of the Cr atoms' d-shells (**Fig. 10a**) and Se atoms' p-shell (**Fig. 10b**) around the Fermi level. The figure illustrates the availability of spin-up states in the supercell. The DOS is significantly increased at ε_f with a P_+ shift. In addition, the spin-down DOS is close to zero for all cases. The asymmetric spin-resolved states near ε_f (between 0.1 and 0.2 eV) indicate a strongly spin-selective electronic response. The DOS gives an indication of the microscopic mechanisms responsible for the observed spin modulation. The corresponding charge-density difference further identifies the spatial regions in which interfacial charge redistribution occurs. Together, these quantities provide a

direct basis for associating the displacement-dependent band modulation with interfacial electronic coupling.

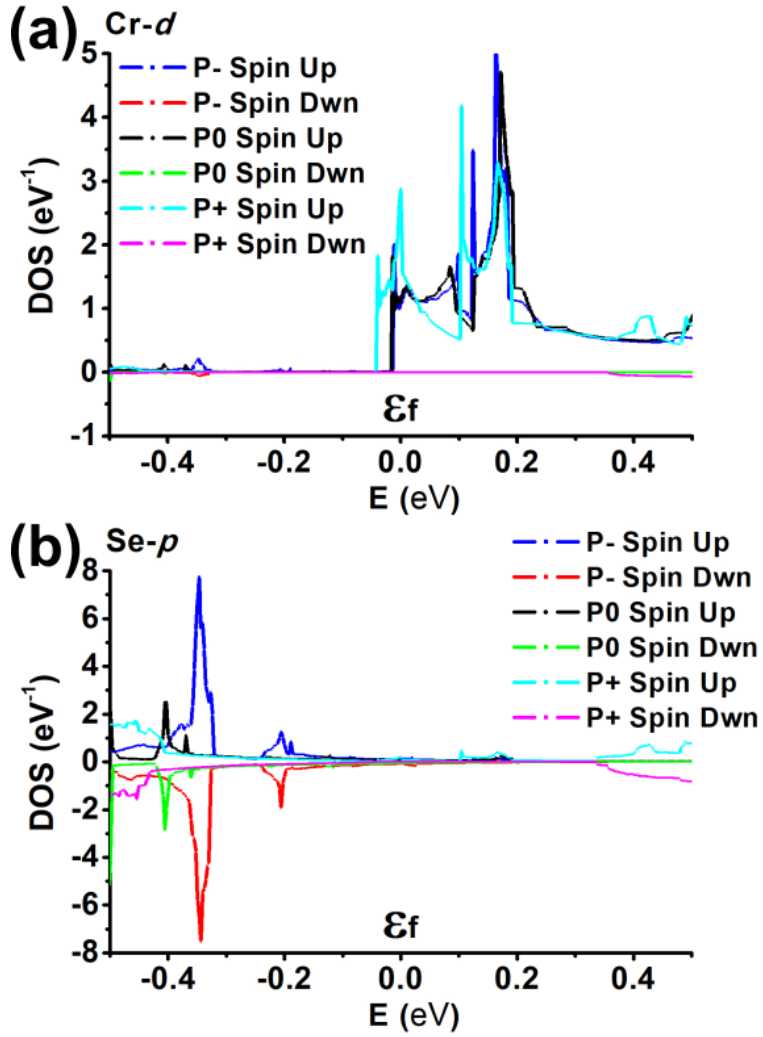


Fig. 10. Combined projected density of states (Fermi level marked ε_f) for P_0, P_+, P_- with spin-up and spin-down polarities. **(a)** Cr atoms' *d*-shells. **(b)** Se atoms' *p*-shells.

CONCLUSIONS

In conclusion, first-principles calculations demonstrate that the proposed In_2Se_4/Cr_2SeO van der Waals heterostructure provides an effective platform for interfacial engineering of altermagnetic electronic states. The heterostructure formation modifies the electronic structure of Cr_2SeO through interfacial charge redistribution and Se-p/Cr-d orbital hybridization, leading to pronounced momentum-dependent changes in the spin-resolved bands. Spin-dependent electronic features of Cr_2SeO are retained while being substantially modulated by the Se-rich In_2Se_4 layer. Overall, the system displays semi-metallic-like properties. The results show that spin-up X bands shift substantially with Se displacement,

while spin-down X bands are comparatively insensitive. In addition, the X-point spin-dependent gap can be strongly modified. These results highlight the potential of chemically engineered chalcogenide interfaces for controlling the electronic and spin-dependent properties of two-dimensional altermagnetic materials and suggest potential relevance for further investigation of In_2Se_4/Cr_2SeO heterostructures in nanoscale spintronic applications.

METHODS

The structure and simulation environment were generated and processed using Synopsys© QuantumATK©.[26, 30] Ball-and-stick diagram figures were generated by UCSF Chimera© [31, 32] and VESTA.[33, 34] Density of states (DOS) calculations were based on the SGGA+U(PBE) algorithm, combining the Spin-polarized Generalized Gradient Approximation (SGGA), the Perdew-Burke-Ernzerhof (PBE) exchange-correlation functional, and an added Hubbard U correction term (+U) with an SCF convergence tolerance of 10^{-7} eV. Ground-state calculations utilized PBE (GGA) basis set functionals within the PseudoDojo framework with medium accuracy. The Coulomb interaction effect was included by using U = 3.55 eV for Cr-3d electrons.[35, 36] The Brillouin zone was sampled with a 15×15×1 k-mesh, while force and stress tolerance levels were set to 0.01 eV/Å and 0.1 GPa, respectively. Calculations were performed using a linear combination of atomic orbitals (LCAO) framework with a density mesh cutoff of 125.0 Hartree. To avoid unphysical interactions between neighboring cells, a 20 Å vacuum gap was added along the c-axis. Long-range van der Waals (vdW) interactions were modeled using the built-in Grimme DFT-D3 semi-empirical dispersion correction with a maximum neighbor distance of 10 Å.

SUPPLEMENTARY MATERIAL

Supporting information is presented online in a general-purpose repository and available from the publisher.

AUTHOR INFORMATION

Corresponding Authors: *E-mail (D. Berco): danny.barkan@gmail.com

ORCID: Dan Berco: 0000-0003-2902-1422

ACKNOWLEDGMENTS

Author Contributions: D.B conceived the concept, developed the architectural methodologies, implemented the modeling, performed the simulations, created the visualization, and wrote the manuscript. The author would like to thank the technical team at Synopsys© for their support.

Competing Interests: The authors declare no conflict of interest.

Ethics Statement: No animal or human experiments were involved in this study.

Data Availability Statement: The data that support the findings of this study are available on request from the corresponding author.

REFERENCES

1. Šmejkal, L., Sinova, J., Jungwirth, T. Emerging Research Landscape of Altermagnetism. *Phys. Rev. X* 2022, 12, 040501.
2. Šmejkal, L., MacDonald, A. H., Sinova, J., Nakatsuji, S., Jungwirth, T. Beyond Conventional Ferromagnetism and Antiferromagnetism: A Phase with Nonrelativistic Spin and Crystal Rotation Symmetry. *Nat. Rev. Mater*. 2022, 7, 482–496.
3. Bai, L., Feng, W., Liu, S., Šmejkal, L., Mokrousov, Y., Yao, Y. Altermagnetism: Exploring New Frontiers in Magnetism and Spintronics. *Adv. Funct. Mater*. 2024, 34, 2409327.
4. Chen, X., Wang, L., Zhang, J., & Liu, Y. (2026). Interfacial bond tailored altermagnetic tunnel junctions. *Physical Review B*, 113(6), 064412.
5. Zhang, H., Zhou, J., Wu, R., & Li, S. (2026). Spin-valley-mismatched altermagnet for giant tunneling magnetoresistance. *npj Computational Materials*, 12(1), 45.
6. Wang, K., Liang, S., Zhang, T., & Liu, J. (2026). Symmetry-locked six-state control of altermagnetism via sliding ferroelectricity. *Science Advances*, 12(23).
7. Šmejkal, L., Sinova, J., & Jungwirth, T. (2025). Altermagnetic Spin Precession and Spin Transistor. *Physical Review Letters*, 134(12), 126401.
8. Gomez, A. M., Rodriguez, F., & Martinez, L. (2025). Spin transfer torque induced deterministic Néel vector motion in altermagnets. *Physical Review B*, 111(18), 184423.

9. Zhang, X. P., Feng, W., Zhang, R. W., Fan, X., Wang, X., & Yao, Y. (2025). Theory of Anisotropic Magnetoresistance in Altermagnets and Its Applications. *Physical Review Letters*, 135(26), 266706.
10. D. Berco, and D.S. Ang, Recent progress in synaptic devices paving the way toward an artificial cogni-retina for bionic and machine vision. *Advanced Intelligent Systems*, 1, p.1900003 (**2019**).
11. D. Berco, D.S. Ang, and H.Z. Zhang, An optoneuronic device with realistic retinal expressions for bioinspired machine vision. *Advanced Intelligent Systems*, 2, p.1900115 (**2020**).
12. D. Berco, D.S. Ang, and P.S. Kalaga, Programmable photoelectric memristor gates for in situ image compression. *Advanced Intelligent Systems*, 2, p.2000079 (**2020**).
13. D. Berco, and D.S. Ang, Bioinspired Robotic Vision with Online Learning Capability and Rotation-Invariant Properties. *Advanced Intelligent Systems*, 3, p.2100025 (**2021**).
14. D. Berco, C.H. Chiu, and D.S. Ang, Hieroglyphically Supervised Bioinspired Visio-neural Controller. *Advanced Intelligent Systems*, 4, p. 2200066 (**2022**).
15. Khan, I., Bezzerga, D., Marfoua, B., Hong, J. Altermagnetism, Piezovalley, and Ferroelectricity in Two-Dimensional Cr_2SeO Altermagnet. *npj 2D Mater. Appl*. 2025, 9, 18.
16. Ding, W., Zhu, J., Wang, Z., Gao, Y., Xiao, D., Gu, Y., Zhang, Z., Zhu, W. Prediction of Intrinsic Two-Dimensional Ferroelectrics in In_2Se_3 and Other III_2–VI_3 van der Waals Materials. *Nat. Commun*. 2017, 8, 14956.
17. Cui, C., Hu, W.-J., Yan, X., Addiego, C., Gao, W., Wang, Y., Wang, Z., Li, L., Cheng, Y., Li, P., et al. Intercorrelated In-Plane and Out-of-Plane Ferroelectricity in Ultrathin Two-Dimensional Layered Semiconductor In_2Se_3. *Nano Lett*. 2018, 18, 1253–1258.
18. Gu, M., Liu, Y., Zhu, H., Yananose, K., Chen, X., Hu, Y., Stroppa, A., Liu, Q. Ferroelectric Switchable Altermagnetism. *Phys. Rev. Lett*. 2025, 134, 106802.
19. Peng, R., Fang, S., Ho, P., Liu, F., Zhou, T., Liu, J., et al. Ferroelastic Altermagnetism. *npj Quantum Mater*. 2026, 11, 5.
20. Engel, E., 2011. *Density functional theory*. Springer-Verlag Berlin, ISBN 978-3-642-14089-1.
21. P., Geerlings F. De Proft and W. Langenaeker, Conceptual density functional theory. *Chemical reviews*, 103, p. 1793-1874 (**2003**).
22. Berco, D.; Tseng, T. Y. A Comprehensive Study of Bipolar Operation in Resistive Switching Memory Devices. *Journal of Computational Electronics*, 15, 577–585 (**2016**).
23. Berco, D.; Tseng, T. Y. A Stochastic Simulation Method for the Assessment of RRAM Retention Reliability. *Applied Physics Letters*, 107, 253504 (**2015**).
24. S. Froyen, and W.A. Harrison, Elementary prediction of linear combination of atomic orbitals matrix elements. *Physical Review B*, 20, p. 2420 (**1979**).
25. J.W. Mintmire, and B.I. Dunlap, Fitting the Coulomb potential variationally in linear-combination-of-atomic-orbitals density-functional calculations. *Physical Review A*, 25, p. 88 (**1982**).
26. Synopsys QuantumATK ver. W-2023.09 https://www.synopsys.com/quantumatk
27. Perdew, J. P., Burke, K., & Ernzerhof, M. (1996). Generalized gradient approximation

made simple. *Physical Review Letters*, 77(18), 3865–3868.

28. Perdew, J. P., Burke, K., & Ernzerhof, M. (1996). Generalized gradient approximation made simple. *Physical Review Letters*, 77(18), 3865–3868; Erratum Physical Review Letters, 78(7), 1396 (1997).

29. Dudarev, S. L., Botton, G. A., Savrasov, S. Y., Humphreys, C. J., & Sutton, A. P. (1998). Electron-energy-loss spectra and the structural stability of nickel oxide: An LSDA+U study. *Physical Review B*, 57(3), 1505–1509.

30. S. Smidstrup, T. Markussen, P. Vancraeyveld, J. Wellendorff, J. Schneider, T. Gunst, B. Verstichel, D. Stradi, P. A. Khomyakov, U. G. Vej-Hansen, and M. E. Lee, QuantumATK: an integrated platform of electronic and atomic-scale modelling tools. *Journal of Physics: Condensed Matter*, 32(1), p. 015901 (**2019**).

31. E. F. Pettersen, T. D. Goddard, C. C. Huang, G. S. Couch, D. M. Greenblatt, E. C. Meng, and T. E. Ferrin, UCSF Chimera-a visualization system for exploratory research and analysis. *J Comp. Chem*, 25(13), p. 1605-12 (**2004**).

32. UCSF Chimera version 1.16 (https://www.cgl.ucsf.edu/chimera/).

33. K. Momma and F. Izumi, "VESTA 3 for three-dimensional visualization of crystal, volumetric and morphology data," *J. Appl. Crystallogr.*, 44, 1272–1276 (**2011**).

34. K. Momma and F. Izumi, "VESTA: a three-dimensional visualization system for electronic and structural analysis," *J. Appl. Crystallogr.*, 41, 653–658 (**2008**).

35. Guo, S.-D., Guo, X.-S., Cheng, K., Wang, K. & Ang, Y. S. Piezoelectric altermagnetism and spin-valley polarization in Janus monolayer Cr2SO. *Appl. Phys. Lett*. 123, 082401 (**2023**).

36. Guo, P.-J., Liu, Z.-X. & Lu, Z.-Y. Quantum anomalous hall effect in collinear antiferromagnetism. *Npj Comput. Mater*. 9, 1–6 (**2023**).